Microstrutural Features of Magnetic NiCoB Nanoparticles Addition to MgB2 Precursor Powders

Lončarek, Ivana; Tonejc, Anđelka; Skoko, Željko; Novosel, Nikolina; Mustapić, Mislav

Journal article, Published version
Rad u časopisu, Objavljena verzija rada (izdavačev PDF)

Permanent link / Trajna poveznica: https://urn.nsk.hr/urn:nbn:hr:217:103277

Download date / Datum preuzimanja: **2025-01-03**

Microstructural Features of Magnetic NiCoB Nanoparticles Addition to MgB₂ Precursor Powders

Ivana Lončarek,[1] Anđelka M. Tonejc,[1] Željko Skoko,[1,*] Nikolina Novosel,[2] Mislav Mustapić[3]

[1] Department of Physics, Faculty of Science, University of Zagreb, Bijenička cesta 32, HR-10000 Zagreb, Croatia

[2] Institute of Physics, Zagreb, Bijenička cesta 46, HR-10000, Croatia

[3] Josip Juraj Strossmayer University of Osijek, Department of Physiscs, Trg ljudevita Gaja 6, HR-31000 Osijek, Croatia

* Corresponding author's e-mail address: zskoko@phy.hr

Abstract: Magnesium diboride (MgB_2) is a superconductor characterized by interesting properties like rather high superconducting transition temperature T_c = 39 K, long coherence length and low anisotropy. In addition, it has a very simple crystal structure and low density. Those properties make the MgB_2 an ideal candidate for a wide range of applications.

To improve the electromagnetic properties of MgB_2, magnetic nickel-cobalt-boron (NiCoB) nanoparticles (mean grain size 17 ± 3 nm) were added to Mg and B precursor powders and sintered at 650 °C, *i.e.* the temperature of MgB_2 superconductor formation. The nearly spherical NiCoB nanoparticles, as-prepared by the chemical reduction of metallic salts, were amorphous according to previous study. The resulting MgB_2 sample, formed after the sintering at 650 °C, was subjected to detailed microstructural analysis which included the application of various experimental methods: XRD, FE-SEM, EDS, elemental mapping, TEM and SAED. The methods confirmed the formation of new crystal CoNi phase (due to heat treatment at 650°C), consisting of spherical nanoparticles (∼ 6 nm) with tendency to spherical agglomerates formation. Those nanosized magnetic particles (characterized by the single domain magnetic structure and blocking temperature T_B below room temperature), located at MgB_2 grain boundaries, could serve as effective magnetic pinning centers in MgB_2, thus improving its electromagnetic properties.

Keywords: magnesium diboride, CoNi nanoparticles, X-ray diffraction, Rietveld refinement, scanning electron microscopy (SEM), transmission electron microscopy (TEM).

INTRODUCTION

THE MgB_2 is characterized with the simple AlB_2 type hexagonal structure (space group P6/*mmm*). The structure consists of alternating triangular planes of Mg which are separated by honeycomb-net planes of boron, with each Mg atom located at the center of hexagon formed by boron (donating its electrons to the boron planes). The reported values of the unit cell parameters for MgB_2 at room temperature are *a* = 0.3086 nm and *c* = 0.3524 nm.[1] These values are in the middle of the values of lattice parameters for AlB_2-type compounds.

Although the structure of MgB_2 has been identified very early, in 1954,[2] the superconductivity in the MgB_2 was not discovered until 2001.[3] Since the discovery, extensive studies have been made covering its fundamental aspects as well as practical applications.[4–6] Due to rather high

critical temperature T_c (39 K), possibility of operation at temperatures ≥ 20 K in liquid hydrogen or with cryocoolers and relatively low costs of raw material, the MgB_2 represents a promising superconductor for next-generation superconducting application in the temperature range of 20–30 K, where the conventional superconductors cannot operate.[7]

For the purpose of different applications, MgB_2 has been fabricated in bulks, single crystals, thin films, tapes and wires.[8] The major drawback for the application of pure MgB_2 wires is rather low upper critical field B_{c2}(4.2 K) ∼ 18 T and weak flux pinning (which results in a low irreversibility field B_{irr}(4.2 K) ∼ 12 T and low critical current density J_c in high fields). Further, in situ prepared MgB_2 samples are very porous, which additionally decreases J_c and causes inhomogeneity within the sample. Therefore, much effort (including chemical doping, irradiation and

thermomechanical processing) is undertaken to improve its properties. So far, the best results are obtained by addition of nonmagnetic amorphous SiC nanoparticles[9–11] and malic acid.[12] The enhancement is a result of several processes: C substitution for B in MgB_2 crystal structure induces disorder which increases the electron scattering and resistivity and enhances B_{c2}, grain refinement leads to enhancement of grain boundary pinning and nanoprecipitates situated between and/or inside MgB_2 grains serve as core pinning centers. Therefore, changes in composition and structure of MgB_2 bulk sample can result in enhanced electromagnetic performance of such wires. Core pinning at non-superconducting impurities inside MgB_2 bulk sample is efficient at distances of the coherence length ξ. Because of that rather high volume density of added nanoparticles ($\sim$ 10 *w.* %) is needed to achieve effective pinning. On the other hand, considerable amount of non-superconducting phases inside MgB_2 reduces connectivity of MgB_2 grains and has detrimental effect on superconducting properties of the sample. This problem can possibly be avoided by adding magnetic nanoparticles to MgB_2. Magnetic interaction between vortices in MgB_2 superconductor and magnetic nanoparticles dispersed inside MgB_2 sample provides additional mechanism of flux pinning and can be much stronger than that involved in core pinning. Magnetic interaction acts on the length scale of the penetration depth λ and since in MgB_2 λ is larger than ξ, the required volume density of magnetic pins is lower than in case of core pinning on nonmagnetic nanoinclusions. In addition, problems with rather large amount of non-superconducting phases inside MgB_2 sample are also diminished using magnetic pins. To achieve the strongest possible magnetic flux pinning single domain magnetic particles (larger magnetic moment) with coercive field lower than magnetic field of vortices should be used.[13] In this work we used nickel-cobalt-boron (NiCoB) nanoparticles which were earlier synthesized by chemical reduction of metallic salts (the details on the synthesis route can be found in previous work).[14] NiCoB particles were nearly spherical with the amorphous structure[14] and magnetic properties favorable for achieving magnetic flux pinning in MgB_2: they have single domain magnetic structure with blocking temperature below room temperature (*i.e.* they are superparamagnetic at room temperature, which is preferable to avoid agglomeration of particles during mixing of Mg, B and NiCoB powders), considerable saturation magnetization and low coercive field at low temperatures. These properties, along with corresponding nano-sized dimension (and consequently single domain magnetic structure), make the NiCoB particles a very promising candidate for the improvement of the electromagnetic properties of the MgB_2 super-conductor.

It should be noticed that the electromagnetic properties of MgB_2 are highly depended on chemical composition, size and morphology of added nanoparticles. In this work the results on how the addition of magnetic NiCoB nanoparticles (in weight fraction 2.67 %), with mean size diameter 17 ± 3 nm, reflects on the microstructural properties of MgB_2 are reported, including the detailed structural characterization of the constituent phases formed during the preparation *via* powder in tube (PIT) *in situ* method.[15] This work represents a part of systematic study on the effect of magnetic nanoparticles addition to MgB_2, with focus on microstructural and structural analysis of the investigated samples. The study of the influence of the magnetic nanoparticles addition on electromagnetic properties of MgB_2 is given elsewhere.[15–18] The MgB_2 sample, formed after the addition of NiCoB nanoparticles (2.67 *w.* %) to Mg and B precursor powders and sintering at 650 °C, which represent the subject of this research, was chosen due to the observed improvement of critical current density in respect to the MgB_2 sample without the addition of the nanoparticles.[15] Generally, the identification of all phases present in the resulting MgB_2 samples formed after the addition of the nanoparticles with various chemical composition to MgB_2 precursor powders (sintered at various temperatures), along with the determination of their morphologies and dimensions, is crucial in understanding and interpreting the observed changes in the superconducting properties of MgB_2 (either positive or negative ones). Finding out whether they are located on MgB_2 grain boundaries or incorporated into MgB_2 matrix, is of great importance also. It has been reported that the substitution of most doping elements on the Mg or B site lead to the suppression of T_c,[19] while the element and compound addition results in improvement of J_c, as mentioned earlier. Although there are some independent studies present, investigating the MgB_2 samples with the performed addition of NiCoB nanoparticles,[20–22] they are mostly dealing with the effect of the addition of the nanoparticles on superconducting properties of MgB_2. The microstructural analysis is mainly focused on the resulting MgB_2 sample (formed after the addition of the nanoparticles to Mg and B precursor powders and sintering at various temperatures),[20] with relatively poor characterization of the identified constituent phases. The characterization usually ends with quantitative analysis of the sample *via* Rietveld refinement (in form of obtained mass fractions of MgB_2, MgO, and possible Mg if it is present).[20,22] Even when the characterization of NiCoB nanoparticles (prior to the addition of Mg and B precursor powders) is present, there is no information about the size and shape of the phases that are formed from the starting nanoparticles (after the addition to Mg and B precursor powders and sintering at various temperatures).[21] The

only information one can get is confirmation of their existence from XRD measurement without any quantitative data, such as their weight fraction. All of the information, along with the ones for the other formed constituent phases, is relevant for understanding their influence on the growth of MgB$_2$ grains (which is closely related to the MgB$_2$ grain connectivity) in the resulting MgB$_2$ sample. Unfortunately, previous studies investigating the resulting MgB$_2$ samples with the addition of magnetic nanoparticles did not make any correlations of the MgB$_2$ crystallites size in these samples to the MgB$_2$ crystallite size in the MgB$_2$ samples without the addition (sintered with the same procedure as the resulting MgB$_2$ samples with the magnetic nanoparticles, but without the addition of the nanoparticles). On contrary, either the sizes of the MgB$_2$ crystallites in the resulting MgB$_2$ sample (formed after the addition of the nanoparticles to Mg and B precursor powders and sintering at various temperatures) are given,[20] or they do not give any information about the sizes of the crystallites.[21,23–25] The same stands for the MgB$_2$ grain sizes determined from electron microscopy observation (mostly from SEM). This work gives an insight in how the addition of the NiCoB nanoparticles affects the sizes of the grains of the constituent phases and elements present in the resulting MgB$_2$ sample (including the information of size and shapes of constituent crystallites in case of MgB$_2$ grains). Moreover, it offers the information on how the addition reflects on the nanoparticles themselves, since it represents an extension of our previously conducted research of composition and morphology investigation of the as-prepared NiCoB nanoparticles (prior to their mixing with Mg and B precursor powders and sintering at 650 °C). Also, with detailed analysis of the MgO and Mg impurities (including XRD, SEM, EDS, elemental mapping, TEM and SAED), the previously reported problem regarding theirs distinguishing by electron microscopy observations[21] has been encompassed. More important, as shown by the detail study in this work, the distinguishing of constituent phases/elements in resulting MgB$_2$ sample, turned out to be crucial in avoiding the potential difficulties in interpreting the FE-SEM and TEM observations, regarding the spherical crystalline Mg and CoNi particles with very similar dimensions (6.1 ± 0.1 nm and 7.6 ± 0.2 nm, respectively). This observation is of great importance in any further study of MgB$_2$ samples with added nanoparticles, since the nanoparticles are often present in the spherical form as in case of the Mg impurity (which is often formed in these samples, especially in the ones sintered at lower temperatures like 650 °C). It can help in avoiding the possible improper interpretation of SEM and or TEM observations regarding the spherical particles identification (especially in cases when EDS and SAED investigations are not included). On the other hand, this is very important in the interpretation of magnetic measurement results in resulting MgB$_2$ sample also (in a sense of distinguishing the contribution of the nonmagnetic from magnetic phase contribution to the observed changes in electromagnetic properties of MgB$_2$).

EXPERIMENTAL METHODS

NiCoB amorphous nanoparticles were synthesized by the chemical reduction of metallic salts.[14] It should be mentioned that the amounts of ethanol solutions of metallic salts Ni(NO$_3$)$_2$ and CoCl$_2$, along with the one of water solution of reducing agent KBH$_4$, were adjusted to yield the nominal composition NiCoB nanoparticles (NP). Then the mixture of $(1 - x)$Mg : xNP : 2B with x = 0.01 was prepared, which corresponds to 2.67 *w.* % of NiCoB nanoparticles. The powders of boron (Speciality Materials, Inc., USA, 0.02–0.1 μm), NiCoB nanoparticles and magnesium (Tangshan Weihao Magnesium Powder Co., Ltd, China, 400 mesh) were first mixed in mortar, and then in WC ball mill (400 rpm) for 8 hours in argon atmosphere (after wetting with small amount of toluene). The mixed powders were filled in iron tube which was drawn in wires with 1.8 mm diameter (so that transport measurements can be performed).[15] Finally, the prepared wires were enclosed in iron tube and sintered at 650 °C for 1 h in the flowing argon atmosphere (with a heating rate 5 °C min⁻¹), and then left to cool down overnight. The resulting MgB$_2$ sample (further in text noticed as Sample 1) was taken out of the iron tubes in order to perform XRD, FE-SEM and TEM measurements.

The other investigated MgB$_2$ sample, in form of MgB$_2$ sample without the addition of NiCoB nanoparticles (further in text noticed as Sample 2), was synthesized with the same procedure described above, but without the addition of NiCoB nanoparticles to Mg and B precursor powders at the begging of the synthesis procedure, as in case of Sample 1.

The characterization of the constituent phases (elements) present in the investigated samples was performed by X-ray powder diffraction (XRD) at room temperature, using Philips PW 1820 counter diffractometer with monochromatized Cu*K*α radiation (graphite monochromator) in Bragg-Brentano geometry. XRD patterns were recorded in the range 10° < 2Θ < 70°, for twelve hours in case of the Sample 1 and one hour in case of the Sample 2. In both cases the scanning steps were 0.02°, with recording times per step set to 10 s / step and 1 s / step, respectively.

Rietveld refinement of the structures, including the size-strain analysis was performed by Topas-Academic 4.1 software (Coelho Software, Brisbane, Australia, 2010.).

LaB$_6$ was used as the instrumental standard, and TCHZ-PV peak type was used as a profile function. Additionally, the XBroad program[26] was used for the crystallite size calculations in different [*hkl*] directions. In this program especially developed for the size-strain analysis of the XRD line broadening, the instrumental broadening is removed by the use of the deconvolution (Stokes) method. The program performs modified Warren-Averbach method which neglects the strain in the crystal lattice. This approximation is valid in our case because the size/strain analysis performed within the Rietveld refinement showed that there was no strain present in the MgB$_2$ crystal lattice (which is also expected because of the heat treatment of the samples during the synthesis).

Morphology and elemental composition of the nanostructures and microstructures present in the investigated MgB$_2$ samples (Samples 1 and 2) were investigated by field emission scanning electron microscope, JEOL FE-SEM 7000F (resolution 1.2 nm at 15 kV; 3 nm at 1 kV), equipped with an X-ray detector for energy dispersive spectroscopy (EDS) system for microanalysis INCA 350. In order to determine the spatial distribution of the element of interest, in SEM mode of working element mapping of specific region of the samples was performed (with measuring time set to 20 min per element). In the case of Sample 1, the additional structural investigation by transmission electron microscopy (TEM) was performed, accompanied with selected area electron diffraction (SAED), using JEOL JEM-2010 200 kV transmission electron microscope (C_s = 0.5 mm, point-to-point resolution 0.19 nm), with lanthanum hexaboride cathode.

Statistical analysis was performed by the commercial software *Statistica 12*.

RESULTS AND DISCUSSION

XRD and FE-SEM

The XRD pattern for the Sample 1 (*i.e.* the resulting MgB$_2$ sample formed after the addition of NiCoB nanoparticles to Mg and B precursor powders and sintering at 650 °C) is shown in Figure 1 (upper red XRD pattern). The bottom black XRD pattern from the Figure corresponds to the Sample 2 (*i.e.* the MgB$_2$ sample without the addition of the NiCoB nanoparticles). The main features in the XRD patterns of both samples correspond to well defined diffraction maxima of MgB$_2$, followed by the ones of MgO and Mg. In the case of Sample 1, the additional XRD maximum around 2Θ = 44.5° can be observed, indicating the presence of CoNi and/or Ni. Due to small intensity of the maximum (owing to the small amount of the phase) and very similar corresponding Bragg's 2Θ position (44.4° for CoNi and 44.5° for Ni; JCPDS 01-074-5694 and JCPDS 00-
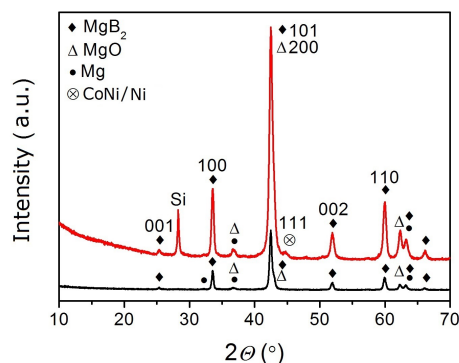

Figure 1. XRD patterns of the Samples 1 and 2.

004-0850, respectively), they cannot be distinguished by certainty. Weight fractions of corresponding phases and elements present in both MgB$_2$ samples, Samples 1 and 2, as well as all the other relevant parameters obtained by Rietveld refinement, are given in Tables 1 and 2, respectively. According to the tables, both samples contain some amount of MgO. The presence of MgO reveals that oxidation of the samples occurred despite of the preparation in the argon atmosphere. This is explained with some amount of oxygen pollution present in the media of inert gas.[27] Water used in preparation procedure of as-prepared sample with NiCoB nanoparticles[14] could also act as a source of oxygen, due to incompletely removing from starting solutions through the argon bubbling. On the basis of previous result published by some of the authors from this work (M. M and Ž. S., Ref. [22]), the small amount of the B$_2$O$_3$ present in the starting semicrystalline boron powder produced at low plasma power (which was also used in the synthesis of the samples performed within this work), observed as a barely visible maximum at 2Θ = 15° in the corresponding XRD pattern,[22] can act as a mediator in forming the MgO. The formation of other oxides in case of the Sample 1, like Co and Ni oxides, is not excluded. However, if formed, such oxides should be present in the amounts being too small to be detected by XRD.

In order to obtain information about the shape of the MgB$_2$ crystallites in the Samples 1 and 2, the calculation of sizes of the crystallites in direction perpendicular to *hkl* reflection planes was performed, via Scherrer and modified Warren Averbach (WA) methods (Table 3). The graphical results of effective size of the MgB$_2$ crystallites (or more precisely, coherent diffraction domains) in the case of the Sample 1, calculated in [100] and [002] crystal directions, as obtained via modified WA method are shown in Figures 2 (a) and (b), respectively. Both methods, Scherrer and modified WA, confirmed that MgB$_2$ crystallites in both samples were longer along the [100] directions (*i.e.* in the direction perpendicular to (100) reflection plane), as shown

in Table 3. By comparing the effective sizes of the crystallites for the Sample 1 with the ones for the Sample 2, it can be seen that the MgB$_2$ crystallites have smaller sizes in the case of the Sample 1. The difference between the Scherrer and WA crystallites size values calculated for the same directions ([100] or [002]), obtained in the case of each of the investigated sample separately, is explained through the fact that the first one represents the plane averaged value while the second one stands for the volume averaged value.

Also, the (effective) sizes of MgB$_2$ crystallites, calculated via Rietveld refinement for both of the

investigated MgB$_2$ samples, 1 and 2; (Tables 1 and 2, respectively), are very close to an average value of the two

Table 2. List of the refined parameters, obtained for the Sample 2.

	Phase / Element		
	MgB$_2$	MgO	Mg
Formula sum	Mg$_{0.93}$B$_{2.0}$	Mg$_{4.0}$O$_{4.0}$	Mg$_{2.0}$
Formula mass / g mol^{-1}	44.2160	161.2176	48.6100
Density / g cm^{-3}	2.5226	3.5720	1.7251
Weight fraction / %	86.3(7)	12.5(5)	1.18(9)
Space group	P6/*mmm* (191)	F*m*$\overline{3}$*m* (225)	P63/*mmc* (194)
Lattice parameters			
a / Å	3.0871(3)	4.2159(4)	3.223(2)
b / Å	3.0871(3)	4.2159(4)	3.223(2)
c / Å	3.5259(3)	4.2159(4)	5.200(5)
a / °	90	90	90
b / °	90	90	90
s / °	120	90	120
Fitting mode (structure fit)			
U	0	0	0
V	0.33(2)	0.28(8)	2.7(8)
W	0.014(8)	0.06(4)	−0.7(2)
Peak shape parameter	0.54(2)	0.83(5)	0.6(0)
R_{exp}			
0.975			
R_p			
0.827			
R_{wp}			
0.119			

Table 1. List of the refined parameters, obtained for the Sample 1.

	Phase / Element			
	MgB$_2$	MgO	Mg	CoNi
Formula sum	Mg$_{0.91}$B$_{2.0}$	Mg$_{4.0}$O$_{4.0}$	Mg$_{2.0}$	Ni$_{4.0}$
Formula mass / g mol^{-1}	43.6911	161.2176	48.6100	234.8000
Density / g cm^{-3}	2.4978	3.5778	1.7320	8.9208
Weight fraction / %	82.4(2)	16.3(2)	1.02(7)	0.24(2)
Space group	P6/*mmm* (191)	F*m*$\overline{3}$*m* (225)	P63/*mmc* (194)	F*m*$\overline{3}$*m* (225)
Lattice parameters				
a / Å	3.0857(2)	4.2137(2)	3.223(2)	3.5223(4)
b / Å	3.0857(2)	4.2137(2)	3.223(2)	3.5223(4)
c / Å	3.5219(3)	4.2137(2)	5.178(8)	3.5223(4)
a / °	90	90	90	90
b / °	90	90	90	90
s / °	120	90	120	90
Fitting mode (structure fit)				
U	0.6(1)	0	0	0
V	−0.1(1)	0.10(6)	0.2(5)	0
W	0.16(3)	0.29(3)	0.2(2)	0.010000
Peak shape parameter	0.71(1)	0.6(0)	0.6(0)	0.6(0)
R_{exp}				
0.038				
R_p				
0.063				
R_{wp}				
0.086				
Size / Å	268	101	73.4	65.8
Strain / %	0.000	0.005	0.017	0.063

Table 3. MgB$_2$ crystallite size, obtained by Scherrer, modified Warren Averbach (WA) and Rietveld methods, for the investigated Samples 1 and 2.

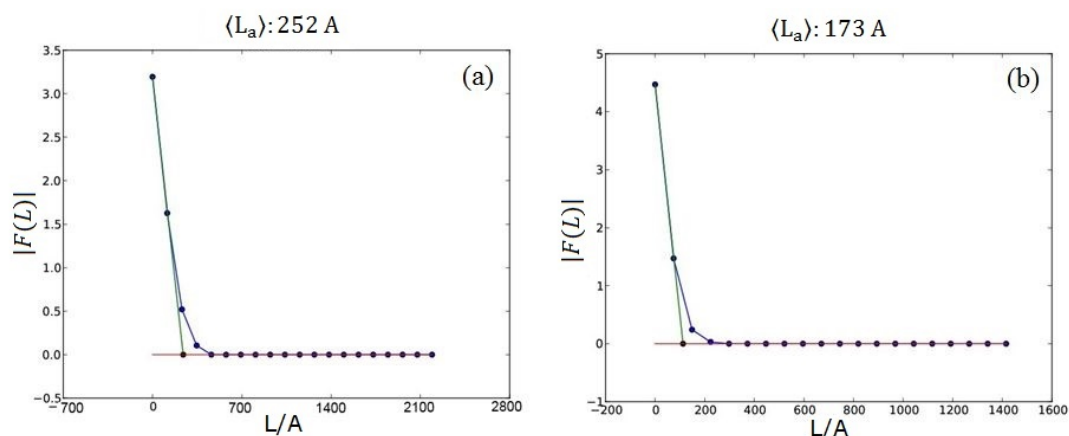|	Scherrer		WA		Rietveld
Sample	[100]	[002]	[100]	[002]	Independent of [*hkl*]
Sample 1	34(1)	22(1)	25.2(3)	17.3(2)	26.6(7)
Sample 2	44(2)	28(1)	34.1(1)	23.7(4)	36.0(7)

Figure 2. Graphical result for the (effective) size of MgB$_2$ crystallites in the Sample 1, obtained via modified WA method. Note: Fourier coefficients (FC) for the selected diffraction maxima *hkl* of pure diffraction profile are shown as blue dots. Tangent on the zeroth FC is shown as green line. The (effective) values of MgB$_2$ crystallites, obtained as the intersection point of the green tangent and the *x*-axis (the red line) for the [100] and [002] crystal directions are shown in (a) and (b), respectively. These sizes, obtained in Å, are displayed at the top of the Figures.
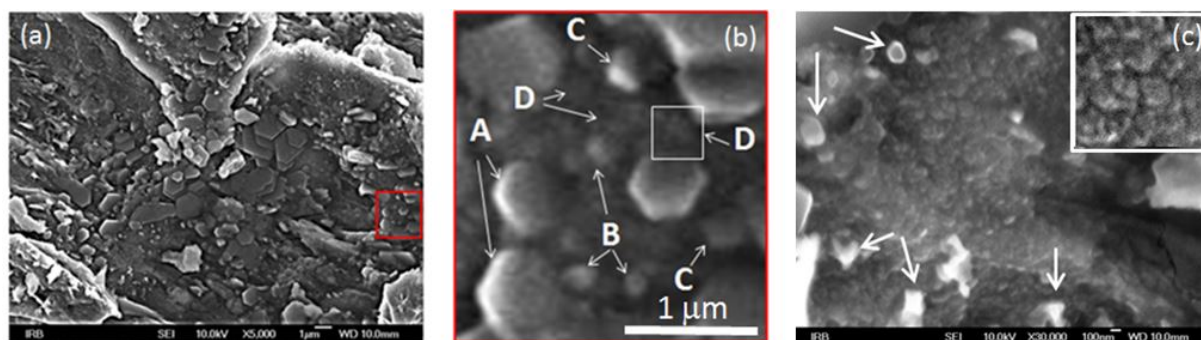
Figure 3. FE-SEM micrographs of one of the investigated regions of the Sample 1 are shown in (a) and (b). Figure (b) represents magnified region of the sample from the marked red square in (a), revealing the presence of four different morphologies: hexagonal shapes A, bright spherical agglomerates B, prism-like shapes C and spherical particles D (forming nearly spherical agglomerates, marked with white square D). The formation of agglomerates formed from spherical particles is also seen in (c), representing different investigated region of the sample rich with those particles (inset in upper right corner, showing magnified region with mentioned agglomerates). Prism-like shapes (white arrows), are also observed in (c).

Scherrer's values regarding the sizes in two different crystal directions, as expected. This is because this method doesn't take into account the size of crystallites along the different crystal directions.

In order to investigate how the addition of NiCoB particles in the MgB$_2$ sample affects the possible changes in lattice parameters of magnesium diboride, the parameter values for the Samples 1 and 2 were calculated *via* Rietveld refinement, and are listed in Tables 1 and 2, respectively. Since no significant change in crystal lattice parameters of these two samples was detected, one can conclude that the incorporation of Co and/or Ni into the MgB$_2$ crystal lattice did not occur. The same conclusion can be made by

introspection of Figure 1, since no displacement of MgB$_2$ diffraction lines 100, 002 and 110 for the Sample 1 in respect to Sample 2, was evidenced. Therefore, it is expected that nanoprecipitates of CoNi and/or Ni, along with ones of MgO and Mg, observed in the XRD pattern of the investigated Sample 1 (upper red XRD pattern in Figure 1), are located at grain boundaries of MgB$_2$. The smaller observed values of MgB$_2$ crystallite sizes in the Sample 1 in respect to the Sample 2, calculated earlier via modified WA and Scherrer methods (Table 3), go in favor to that statement also. This is explained with limited growth of MgB$_2$ grains, due to the formation of earlier mentioned nanoprecipitates at grain boundaries.
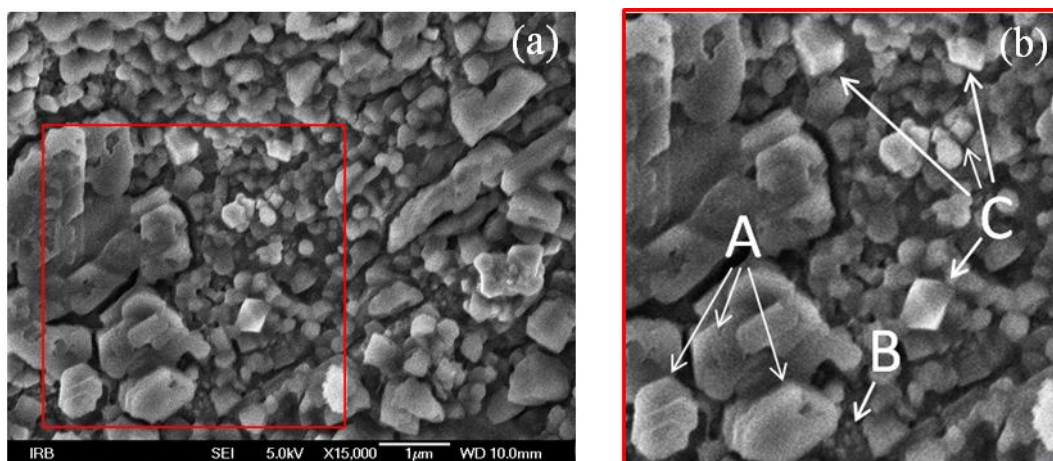
Figure 4. FE-SEM micrograph of the Sample 2, shown in (a). The magnified region of the sample from the marked red square in (a), shown in (b), reveals three different morphologies present in the sample: hexagonal shapes (A), spherical particles (B) and shapes like prisms (C).

Furthermore, the mean size of hexagonal shapes for both MgB_2 samples (Samples 1 and 2), which should correspond to MgB_2 grains according to study from our previous works,[16,17] was determined from FE-SEM micrographs, as shown in Figures 3 (a) and 4 (a), respectively. The size distributions of corresponding measured diameters of hexagonal grains are shown in Figures 5 and 6. According to the Figures the mean size of the grains is approximately the same in both investigated MgB_2 samples, *i.e.* in the Sample 1 (290 ± 20 nm) and the Sample 2 (230 ± 60 nm). Still, one can observe that there is a tendency of forming slightly bigger hexagonal grains in the Sample 1. It should be noticed that beside of the mentioned hexagonal shaped grains (A in Figure 3 (b)), other morphologies in form of bright spherical agglomerates (B in Figure 3 (b)), prism-like shapes (C in Figure 3 (b)), and spherical particles (D in Figure 3 (b)), were also observed in the Sample 1. As can be seen with closer inspection of Figure 3 (b), the spherical particles D form nearly spherical agglomerates (marked with white square). The mean diameters of brighter spherical agglomerates B, and darker nearly spherical agglomerates made of particles D, are about 34 nm and 20 nm, respectively, as estimated from Figure 3 (b). The better overview of nearly spherical agglomerates consisting of the spherical particles is observed in FE-SEM micrograph of different investigated area of the sample, rich with those nanoparticles (Figure 3 (c)). The closer look of the inset in Figure 3 (c) in upper right corner (marked with white square), corresponding to magnified region of the part of the Figure, reveals that the mentioned agglomerates form even bigger nearly spherical agglomerates. The main diameters of these agglomerates measured from Figure 3 (c), are 20 ± 3 nm, for the smaller ones, and 150 ± 10 nm, for the bigger ones. It should be
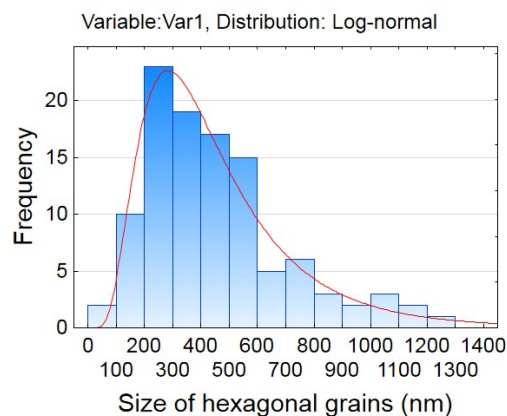

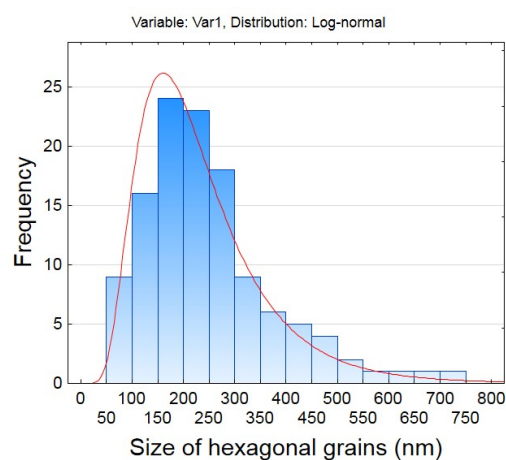**Figure 5.** Size distribution of the hexagonal grains for the Sample 1.

Figure 6. Size distribution of the hexagonal grains for the Sample 2.
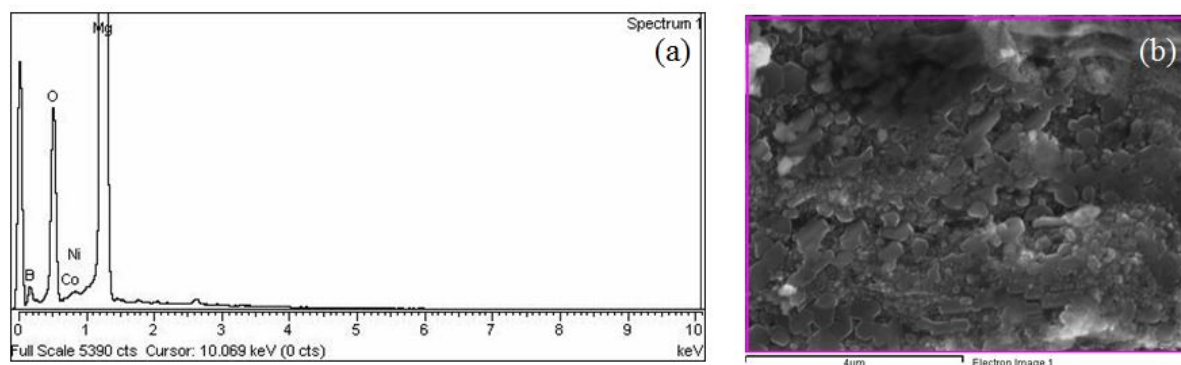
Figure 7. EDS spectrum of the Sample 1 (a), taken from a region of the sample shown in (b).
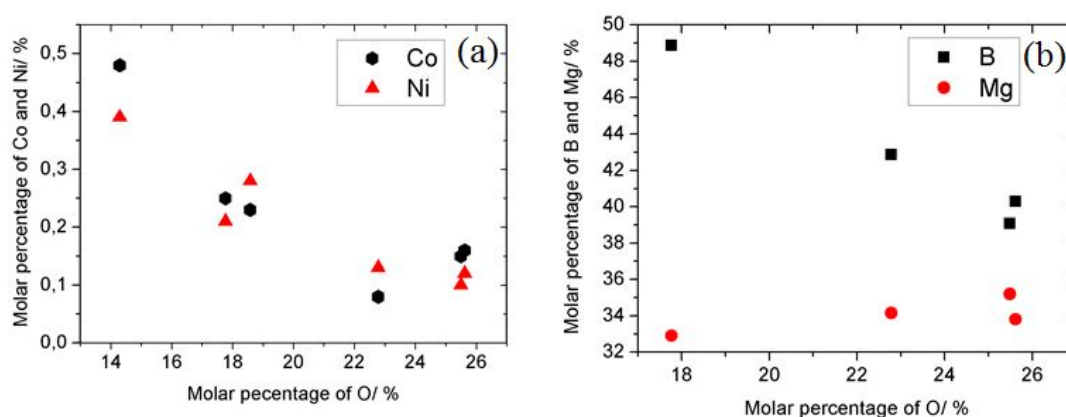

Figure 8. Molar percentage of Co (black hexagon) and Ni (red triangle) plotted against the molar percentage of oxygen (a). Molar percentage of B (black square) and Mg (red sphere) plotted against the molar percentage of oxygen is shown in (b). Both (a) and (b) were measured for the Sample 1.

mentioned that shapes like prisms are also observed in the region rich with spherical particles (white arrows in Figure 3 (c)). The measured dimensions of the marked prisms were in the range 150–240 nm (with the mean size value 200 ± 20 nm).

According to Figure 4 (b), the Sample 2 is also composed of hexagonal shaped grains (A) as expected, but there are also present very small amount of spherical particles (B) with mean diameter 43.7 ± 0.8 nm. The prism-like shapes (C) are also observed, as for the case of Sample 1, but with smaller mean diameter (140 ± 6 nm) in respect to the one observed in the Sample 1. Generally, the measured dimensions of MgO were smaller in the case of the Sample 2, ranging 70–200 nm.

EDS Analysis and Elemental Mapping

EDS spectrum (Figure 7 (a)) of a specific region with four different morphologies present in Sample 1 (Figure 7 (b)), like the ones earlier seen in Figure 3 (b), reveals that the sample is composed of Mg, B, Co and Ni (E ($K\alpha_1$) = 1,254 keV;

E ($K\alpha_1$) = 0,185 keV; E ($L\alpha_1$) = 0,775 keV; E ($L\alpha_1$) = 0,849 keV, respectively), as expected. The additional presence of O ($E(K\alpha_1)$ = 0,523 keV) indicates that the oxidation of the sample had occurred, as this is confirmed earlier by quantitative phase analysis via Rietveld refinement (Table 1). Very small amount of detected Cl (($E(K\alpha_1)$) = 2,622 keV) is explained as a remnant from synthesis of NiCoB particles (due to the $CoCl_2$ metallic salt used in the preparation procedure).[14] Quantitative EDS analysis of the region shown in Figure 7 (b) indicates the presence of MgB_2 and MgO, along with some amount of unreacted Mg. Small amount of detected Co and Ni, with molar Co:Ni ratio close to 1 : 1, indicates the presence of CoNi, as well. This is in very good agreement with earlier XRD observations (Figure 1; Table 1). In order to investigate if there is a tendency towards forming Co and Ni oxides, the molar percentage of Co and Ni against the molar percentage of O (Figure 8 (a)), measured in several selected EDS windows of different regions of the investigated sample was plotted. This EDS analysis revealed that the larger molar percentage of the

elements occur in the oxygen poor EDS windows. Therefore, Ni and Co oxides were not prevalent oxide phases formed in the investigated sample. The small molar percentage of Ni and Co (below 0.2 %), which occur in the oxygen rich EDS window, indicate that the very small amount of Ni and Co oxides could have been formed (*i.e.* in the amount being too small to be detected by XRD). It should be noticed that the largest measured molar percentages of Co and Ni (0.47 % and 0.39 %, respectively), shown in selected EDS window against the oxygen content from the Figure 8 (a), correspond to the specific region rich with the spherical particles (as the one in Figure 3 (c)). Thus these spherical particles could represent CoNi nanoparticles. The average molar Co:Ni ratio, calculated from the detected Co and Ni percentages in the Figure 8 (a) (*i.e.* the detected Co and Ni percentages from several investigated region of the sample) of value 1.1 ± 0.1 support this statement also. Furthermore, by comparing the mean size of bigger spherical agglomerates from Figure 3 (c), which consist of smaller spherical agglomerates made of the mentioned spherical nanoparticles, with the one given in literature for CoNi alloy,[28] it can be seen that there is a very good agreement between the two (Table 4). Spherical morphology of CoNi, as observed in that case also, as well as the tendency of formation spherical agglomerates. It is reported that sizes of CoNi agglomerates depend on Co fraction in the alloy, growing with the Co fraction increasing. This could explain somewhat larger sizes in case of CoNi agglomerates from literature,[28] Table 4. Also, the measured mean size of bigger spherical agglomerates from Figure 3 (c), corresponds to the one observed for smooth spherical agglomerates in annealed sample with NiCoB nanoparticles from our previous work[14], Table 4, which were mostly composed of Co and Ni. These agglomerates were also formed as a consequence of annealing at 650 °C, but their quantity was too small to be identified with certainty as CoNi agglomerates by XRD.

Table 4. Comparison of mean diameters of bigger spherical agglomerates from Figure 3 (c), representing the Sample 1, with the one measured in the case of spherical CoNi agglomerates from literature[28] and the one for smooth spherical agglomerates from our previous work.[14] Note: mean diameter value for CoNi alloy from literature is given for the case of $Co_{53}Ni_{47}$ alloy, *i.e.* the one with closest Co:Ni ratio value to 1 : 1, as in case of the observed ratio in previous work.[14]

Sample	Mean diameter of spherical agglomerates / nm
Sample 1	150 ± 10
CoNi[litreature][28]	175 ± 37
NiCoB (annealed)[14]	150 ± 11

The small amount of unreacted Mg (the presence of which is explained by slow atomic diffusion in solid-solid reaction at 650 °C,[29] *i.e.* at temperature at which the Sample 1 was synthesized), implies that some small amount of unreacted B and/or some kind of B oxide could be present also. The formation of the oxide depends on the amount of the remaining oxygen (which was not included in the formation of MgO). If formed, such oxides should be present in the amounts being too small to be detected by XRD, hence they are not present in the XRD pattern of the sample. According to the Figure 8 (b), showing the molar percentages of B and Mg plotted against the molar percentage of O, which were measured in several selected EDS windows of different regions of the investigated sample, the molar percentage of B decreases with the increasing molar percentage of O. On the contrary, the measured molar percentage of Mg shows the opposite trend: it increases with the increasing molar percentage of O. This implies that the MgO is formed as a prevalent oxide phase in the investigated sample, as this is confirmed by quantitative phase analysis via Rietveld refinement, Table 1. It should be mentioned, that the maximal molar percentage of B (48.86 %), which corresponds to the minimal molar percentage of O and Mg in the Figure (17.77 % and 32.91 %, respectively) was measured from the selected region of the sample with completely different morphology (in respect to all other ones observed in various regions of the sample), present in a form of large irregular micrometer agglomeration. Figure 9 (a) shows the EDS spectrum of the region containing the irregular agglomeration (Figure 9 (b)). This observed surplus of B indicates that the agglomeration represents the residual from the sample preparation in form of unreacted boron. On the other hand, while interpreting of the smaller molar ratio of B occurred in the oxygen and magnesium rich EDS window (corresponding to regions of the sample consisting of regular morphologies observed in the sample) one has to be very careful. Majority of the observed oxygen is that from the formed MgO (as explained earlier), while the majority of the observed boron in the magnesium rich area is that from the formed MgB_2 (as confirmed by quantitative phase analysis via Rietveld, Table 1). Therefore, if some boron oxides exist in the sample, they are present in the amount which is too small to be detected by XRD.

The local EDS spectra of hexagonal and prism-like shapes (like the ones shown in Figures 3 (a) and (b)) revealed that they correspond to MgB_2 and MgO, respectively, as observed in case of Sample 2 also (not shown within the manuscript).

In order to investigate the spatial distribution of the detected elements in the investigated Sample 1, the elemental mapping of the region of the sample comprising of earlier mentioned morphologies, was performed (Figure
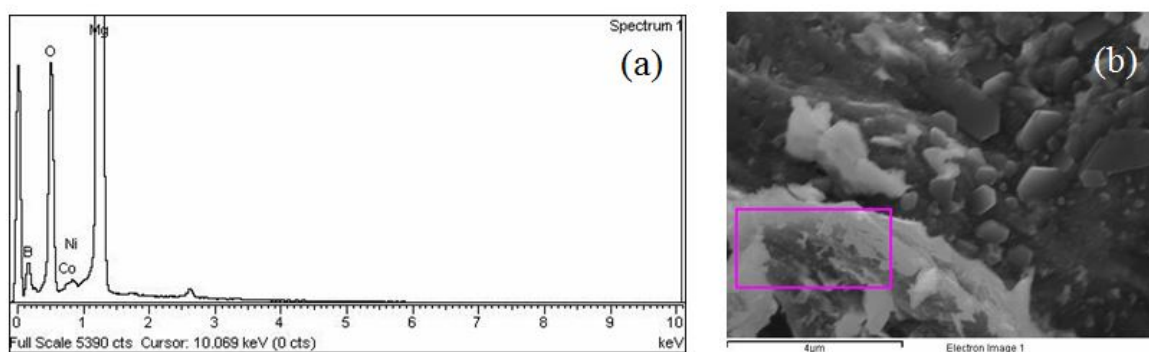
Figure 9. EDS spectrum (a) of the selected region of the Sample 1, containing completely different morphology (large micrometer agglomeration) in respect to all other ones observed in the sample (b). The measuring bar is 4 μm.
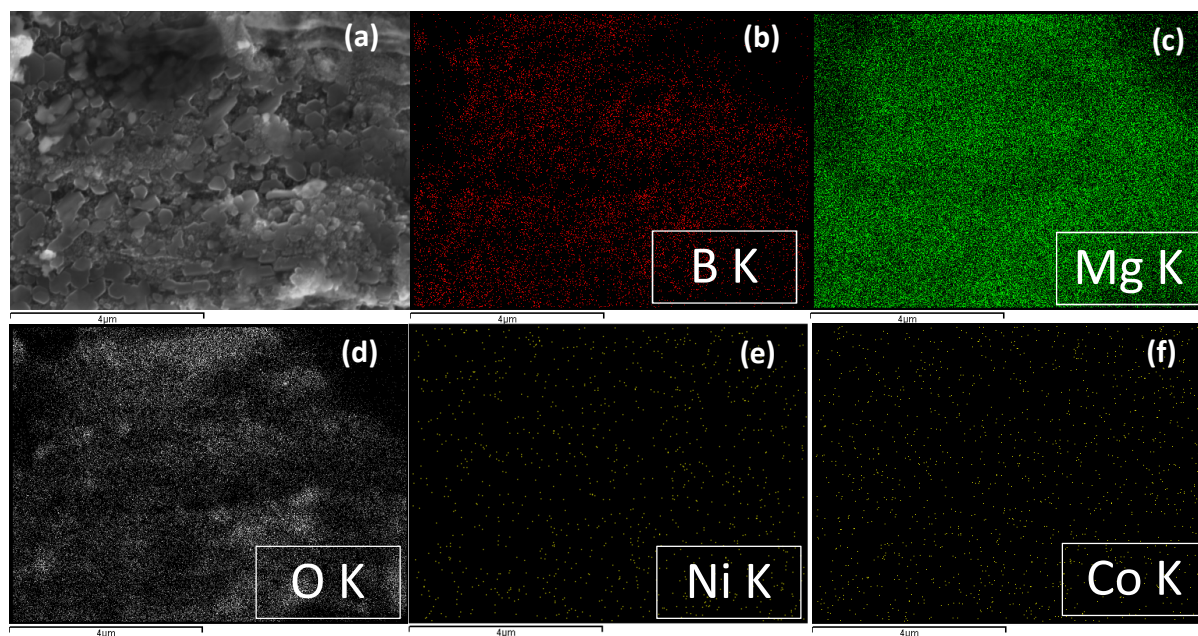

Figure 10. FE-SEM micrograph of the region of Sample 1 (a) used for elemental mapping, and element maps for B (b), Mg (c), O (d), Ni (e) and Co (f). The measuring bar is 4 μm.

10 (a)). The related maps of the constituent elements of the investigated sample are shown in Figures 10 (b), (c), (d), (e) and (f). By comparing Figures 10 (a), (b) and (c), one can see that hexagonal shapes are composed of B and Mg (with Mg present in larger mass concentration). A closer inspection of Figure 10 (d) reveals the presence of smaller amount of O, concentrated in specific regions that correspond to the ones with larger concentration of Mg in Figure 10 (c). These overlapping regions with larger Mg and O concentrations correspond to MgO prisms in Figure 10 (a), observed as brighter in respect to MgB_2 hexagons. This is in a good agreement with earlier XRD and EDS observations. The observed surplus of detected Mg (Figure 10 (c)), is

explained as a remnant from incomplete synthesis reaction of MgB_2.

It should be mentioned also that unlike of the confirmation of presence of MgB_2 hexagons, MgO prisms and the indication of presence of the spherical CoNi particles (throughout the parallel FE-SEM and EDS analysis), the morphology of Mg (the presence of which was confirmed from earlier XRD observations), was not determinated. Therefore, the FE-SEM micrograph of the region of the sample at which elemental mapping was performed (Figure 10 (a)), was closely investigated in order to determine the morphology of detected surplus of Mg (Figure 10 (c)). In other words, one had to determine the
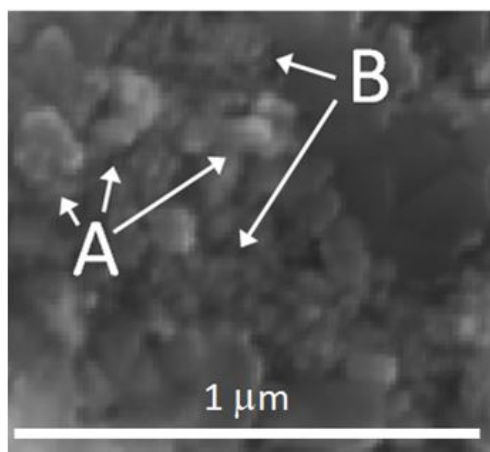
Figure 11. The magnified lower right region of the sample shown in Figure 10 (a), reveals the presence of two different spherical morphologies: the brighter nearly spherical agglomerates forming bigger nearly spherical agglomerates (A), as well as the darker spherical particles which form spherical agglomerates joining in even bigger spherical agglomerates (B).

existence of different morphology in respect to earlier observed ones for MgB_2, MgO and CoNi. Magnified lower right part of the Figure 10 (a), corresponding to the region with bigger concentration of Mg, from the lower right region of the Figure 10 (c), reveals the presence of nearly spherical agglomerates which form even bigger nearly spherical agglomerates (A in Figure 11). These agglomerates appear as brighter in respect to the spherical particles marked with B in Figure 11, which also show tendency of forming spherical agglomerates. It should be noticed that the morphology and size of darker spherical agglomerates made of smaller spherical particles (B in Figure 11), with tendency of forming even bigger spherical agglomerates, correspond to the ones earlier observed for the spherical agglomerates in Figure 3 (c), *i.e.* to the agglomerates with the strong indication that it is about of CoNi agglomerates, Table 5. Therefore the brighter nearly

spherical agglomerates, which form bigger nearly spherical agglomerates A in Figure 11, with mean size around 36 nm (as estimated from the Figure), should correspond to Mg. To this in favor also go XRD and FE-SEM observations in the case of Sample 2, regarding the spherical entities (earlier characterized as nanoparticles due to lower resolution) in Figure 4 (b), with somewhat bigger size of $\sim$ 44 nm (Table 5), which were identified as Mg (as this was additionally confirmed by EDS and elemental mapping observations of the sample, not shown within the manuscript). Slightly minor size of the Mg agglomerates observed in the Sample 1, supports the earlier statement of theirs settlement at the grain boundaries. Also, if one compares the morphology and size of brighter Mg agglomerates, forming bigger nearly spherical Mg agglomerates A in Figure 11, with the ones of fourth unidentified morphology in Figure 3 (b), regarding the bright spherical agglomerates B with size about 34 nm, it can be seen that very good agreement is accomplished (Table 5). With closer inspection of Figure 3 (b), it can be seen that the bright Mg agglomerates (B), along with the MgO prisms and CoNi agglomerates made of spherical particles (C and D, respectively) are located at MgB_2 grain boundaries, as this is claimed earlier.

Furthermore, by comparing the element maps for Ni and Co (Figures 10 (e) and 10 (f)), it can be seen that they share very similar spatial distribution and are present in similar concentrations (as observed from earlier quantitative EDS analysis). The detailed investigation of spatial distribution of Ni and Co from corresponding maps was performed in other study.[15] The spatial distribution which differs from random in form of some local deviations goes in favor to the formation of CoNi particles.

TEM and SAED

With closer inspection of TEM bright field (BF) image of Sample 1 (Figure 12 (a)), one can see that along with a large grain A of length 300 nm and width 200 nm, much smaller dark and bright spherical particles are present also (with observed tendency of forming spherical agglomerates in both cases). The mean diameter of darker particles,

Table 5. The list of measured diameters of the spherical morphologies observed in the corresponding FE-SEM micrographs for the Samples 1 and 2.

Sample	Figure with present morphology	Present morphology	Mean diameter / nm
Sample 1	Figure 3 (b)	Brighter spherical agglomerates B	34
		Spherical agglomerates made of darker spherical particles D (white square)	20
	Figure 3 (c)	Smaller agglomerates made of darker spherical particles → CoNi particles	20
	Figure 11	Brighter spherical agglomerates A	36
		Darker spherical agglomerates B	20
Sample 2	Figure 4 (a)	Bright spherical Mg entities	44

measured from Figure 12 (a), is 6.1 ± 0.1 nm, while the mean diameter of spherical agglomerates of these particles is 21 ± 1 nm, as measured from the same Figure. The corresponding distributions of measured diameters are shown in Figures 13 (a) and (b), respectively.

If one looks at Table 6, showing the values of measured mean diameters for the case of darker spherical nanoparticles from TEM BF micrograph in Figure 12 (a), along with the ones obtained from previously FE-SEM observations, it can be seen that the TEM diameter values
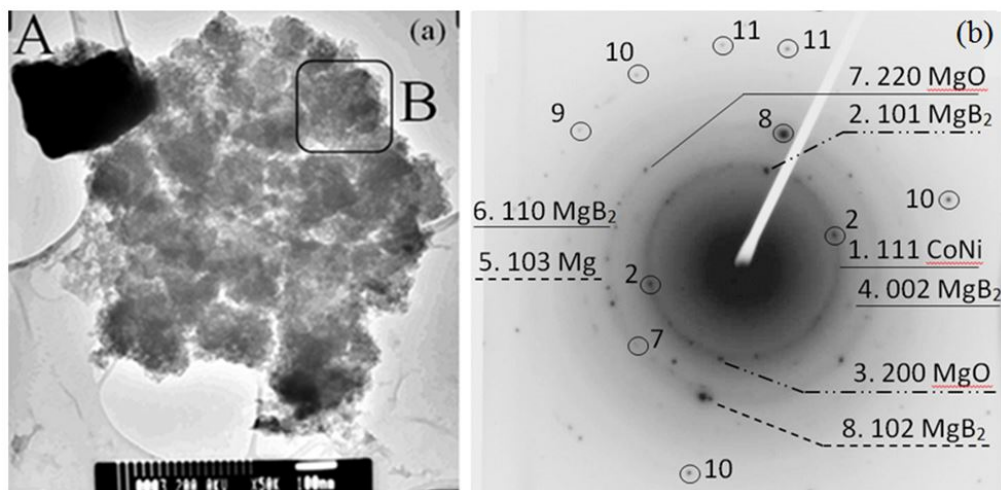

Figure 12. TEM bright field (BF) micrograph for the Sample 1 (a), taken with 50K magnification (measuring bar is 100 nm). Corresponding electron diffraction from the selected area in (a), SAED, is shown in (b).

Table 6. The list of the measured mean diameters for the observed spherical morphologies formed in case of darker spherical nanoparticles in the Sample 1, obtained from TEM (Fig. 12 (a)) and FE-SEM (Figure 3 (c)).

	Mean diameter / nm				
	TEM		FE-SEM		
Sample	Spherical particles	Agglomerates which are formed from spherical particles	Bigger agglomerates which are formed from smaller agglomerates made of spherical particles	Spherical agglomerates which are formed from spherical nanoparticles	Bigger agglomerates which are formed from smaller agglome-rates made of spherical particles
Sample 1	(6.1 ± 0.1)	(21 ± 1)	(100 ± 10)	(20 ± 3)	(150 ± 10)

Table 7. The list of the results obtained from SAED in Figure 12 (b), for the Sample 1.

	Phase									Phase and/or element	
	Observed in form of black spots marked with numbers									Observed in form of rings marked with numbers	
	MgB$_2$	MgO	MgB$_2$	MgB$_2$	MgO	MgB$_2$	MgO	MgO	MgB$_2$	CoNi	Mg
	2	3	4	6	7	8	9	10	11	1	5
Calculated d_{hkl} from SAED (Fig. 9 (b))	1.129	2.106	1.767	1.544	1.491	1.469	0.963	0.943	0.931	2.039	1.473
(*hkl*)	(101)	(200)	(002)	(110)	(220)	(102)	(331)	(420)	(113)	(111)	(103)
d_{hkl} from ICCD-PDF database	1.128	2.107	1.761	1.542	1.490	1.470	0.966	0.942	0.933	2.040	1.473
(*hkl*)	(101)	(200)	(002)	(110)	(220)	(102)	(331)	(420)	(113)	(111)	(103)
Number of card from SCCD-PDF database	01-074-0982	01-087-0653	01-074-0982		01-087-0653	01-074-0982	01-087-0653		01-074-0982	01-074-5694	00-035-0821

Variable: Var1, Distribution: Log-normal

(a)

Spherical particle size distribution (nm)

Variable: Var 1, Distribution: Log-normal

(b)

Size distribution of smaller spherical
agglomerates(nm)

Variable: Var1, Distribution: Log-normal

(c)

Size distribution of bigger nearly
spherical agglomerates composed
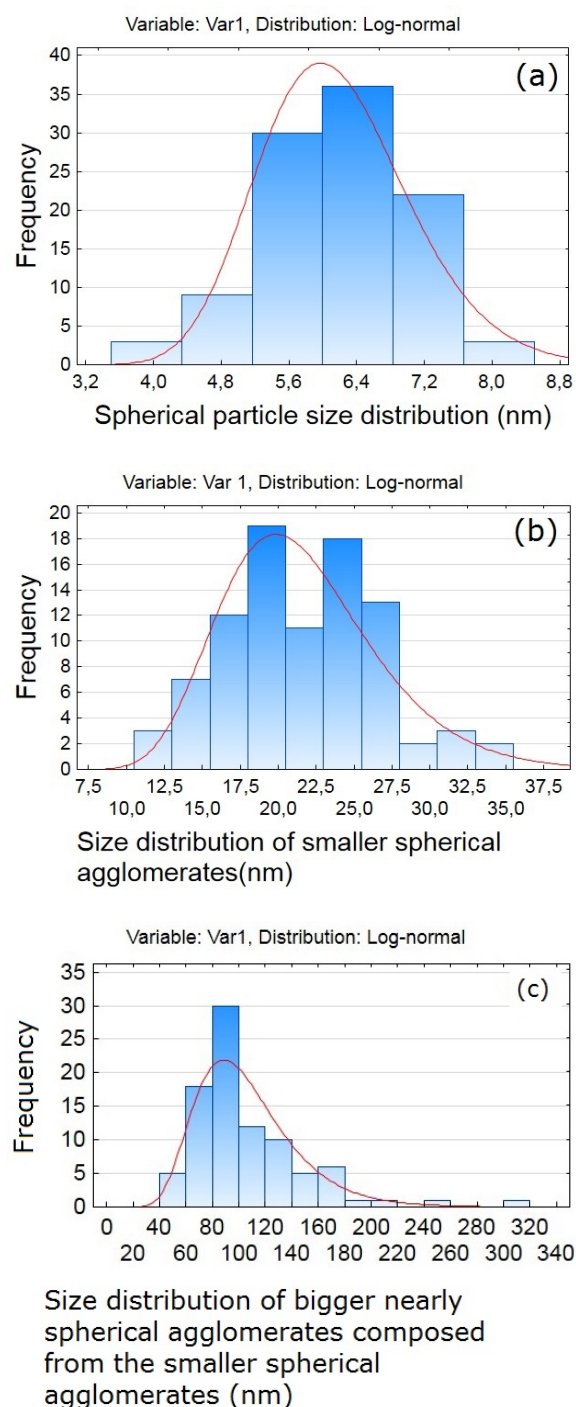from the smaller spherical
agglomerates (nm)

Figure 13. Size distribution of the darker spherical particles (a), along with the one for the spherical agglomerates made of the darker spherical particles (b). Figure (c) shows size distribution of bigger nearly spherical agglomerates, which are composed from the smaller spherical agglomerates (the dimensions of which are shown in (b)). All of the represented size distributions were obtained from TEM BF micrograph for the Sample 1, shown in Figure 12 (a).

for spherical agglomerates (21 ± 1 nm), which form much smaller spherical particles (~ 6 nm), are in very good agreement with the ones previously observed from FE-SEM (20 ± 3). This also stands for the measured diameters of bigger spherical agglomerates consisting of those smaller spherical agglomerates: 100 ± 10 nm (Figure 13 (c)), for the ones like B from TEM micrograph in Figure 12 (a), and 150 ± 10 nm, for the ones from previous FE-SEM micrograph in Figure 3 (c).

In order to identify the observed morphologies, the electron diffraction of corresponding selected area of the investigated sample (SAED) was performed (Figure 12 (b)). According to SAED observation from Table 7, the two diffraction rings 1 (the one with higher intensity) and 5 (the one with lower intensity), correspond to crystalline CoNi and Mg nanoparticles, respectively. It should be noticed that the CoNi particles appear darker in respect to brighter Mg particles (Figure 12 (a)), due to the bigger contrast in case of the elements with larger atomic numbers: Z (Ni), Z (Co) > Z (Mg). The observations from BF TEM (Figure 12 (a), Table 6) and SAED (Table 7), are in very good agreement with previous FE-SEM and EDS observations, regarding the identification of darker CoNi spherical particles which form spherical agglomerates (D in Figure 3 (b)), joining in even bigger spherical agglomerates (white square in Figure 3 (c)), as well as with the identification of brighter nearly spherical Mg agglomerates (B in Figure 3 (b)). This SAED observation also shows that such method is an excellent complementary method to the XRD. XRD results were not conclusive in regard to the distinction between CoNi or Ni phase, but the SAED results definitively confirm the presence of the CoNi phase in the sample. According to TEM observation in Figure 12 (a), the measured sizes of spherical particles forming both kinds of mentioned agglomerates are 6.1 ± 0.1 nm in case of CoNi particles, and 7.6 ± 0.2 nm in case of Mg particles. If one compares the mean size of spherical CoNi particles Sample 1 (6.1 ± 0.1 nm), with the mean size of amorphous spherical particles in the as-prepared sample with NiCoB nanoparticles from previous work[14] (17 ± 3 nm), it can be seen that the spherical CoNi particles from present work are characterized with much smaller values. Nevertheless, the CoNi particles show strong tendency towards forming of the spherical agglomerates with the dimensions up to ~ 100 nm. The formation of such agglomerates (not observed in the case the as-prepared sample with NiCoB nanoparticles)[14] is explained with the change in the corresponding magnetic properties, which occurred because of the microstructural changes due to the annealing of the sample at 650 °C.

Furthermore, with closer inspection of Figure 12 (b), the black spots which correspond to particles with large dimensions can be observed also. The highest intensity

spots marked with 2 and 8, which correspond to the biggest particles (*i.e*. A in Figure 12 (a)), are identified as MgB$_2$ (Table 7). Also, black spots located just outside the ring 1 (like the one numbered with 3), which correspond to MgO particles (Table 7), are overlapping with spots numbered with 2 (*i.e.* spots identified as MgB$_2$). This is denoted in a way that both measured d_{hkl} values of corresponding phases are labeled with the same blue color in the Table. One can see that the SAED observation is in a very good agreement with the previous one from XRD (Figure 1), regarding the overlapping of the 101 and 200 diffraction lines, near the Bragg's angle $2\varTheta \approx 42°$ (*i.e.* the diffraction lines with the highest intensity, identified as MgB$_2$ and MgO). The same situation is observed for the ring 5 in Figure 12 (b), which corresponds to Mg (Table 7), and the high intensity black spots numbered with 8, identified as MgB$_2$ (as from XRD observation in Figure 1, regarding the overlapping of 103 Mg and 102 MgB$_2$ diffraction lines near the Bragg's angle $2\varTheta \approx 63°$). This is denoted in a way that both measured d_{hkl} values of corresponding phase/element are labeled with the same red color in the Table.

The black spots numbered with 4, 6, 8 and 11 (Figure 12 (b)), corresponding to the particles of bigger dimension, are identified as MgB$_2$, while the ones which correspond to big MgO particles are numbered with 7, 9 and 10 (Table 7). Also, although the MgB$_2$ and MgO, along with Mg, are observed in a lot of other different values of Bragg's angle, only ones with the high intensity were marked with numbers for better overview.

CONCLUSION

The detailed study of the resulting MgB$_2$ sample formed after the addition of NiCoB nanoparticles (2.67 *w.%*) to Mg and B precursor powders and sintering at 650 ° (Sample 1), revealed the formation of new crystal CoNi phase as a consequence of the heat treatment at 650 °C. The presence of the CoNi was confirmed with SAED (Figure 12 (b); Table 7). This observation is in very good agreement with the ones obtained from quantitative EDS analysis and elemental mapping, according to which the constituent elements Ni and Co are present in average atomic ratio 1.1 ± 0.1, with similar spatial distribution and concentration along the investigated sample (Figures 10 (e) and (f)).

The spherical nanoparticles of CoNi, with size ~ 6 nm (as confirmed with TEM and SAED observations; Figures 12 (a) and (b), respectively), prone to the formation of the spherical agglomerates, were located at MgB$_2$ grain boundaries. This can be clearly seen from FE-SEM observation (D in Figure 3 (b)), as well as from the Rietveld refinement results for *a* and *c* unit cell parameters for the Sample 1 and the Sample 2 (*i.e.* the MgB$_2$ sample without the addition of the nanoparticles), shown in Tables 1 and 2,

respectively. The lack of any significant change in the parameter values of the two samples suggests that the incorporation of Ni and Co into crystal structure of MgB$_2$ did not occur. To this in favor also go the decreased values of the (effective) MgB$_2$ crystallites sizes in the Sample 1 (as observed *via* modified Warren Averbach, Scherrer and Rietveld methods), in respect to the Sample 2. The settlement of CoNi spherical particles at grain boundaries, along with the MgB$_2$ hexagons, MgO prisms, and Mg spherical particles could explain the inhibited growth of the crystallites.

REFERENCES

[1]   Y. Sun, D. Yu, Z. Liu, T. Wang, J. He, J. Xiang, D. Zheng, Y. Tian, *Supercond. Sci. Technol.* **2007**, *20*, 261.

[2]   M. E. Jones, R. E. Marsh, *JACS* **1954**, *76*, 1434.

[3]   J. Nagamatsu, N. Nakagawa, T. Muranaka, Y. Zenitani, J. Akimitsu, *Nature* **2001**, *410*, 0028.

[4]   C. Buzea, T. Yamashita, *Supercond. Sci. Technol*. **2001**, *14*, R115.

[5]   E. W. Collings, M. D. Sumption, M. Bhatia, M. A. Susner, S. D. Bohnenstiehl, *Supercond. Sci. Technol*. **2008**, *21*, 103001.

[6]   A. Gurevich, *Physica C* **2007**, *456*, 160.

[7]   C. Shekhar, R. Giri, R. S. Tiwari, O. N. Srivastava, *Cryst. Res. Technol.* **2004**, *39,* 718.

[8]   M. Eisterer, H. W. Weber, *Trans. Appl. Supercond.* **2009**, *19*, 2788.

[9]   O. Husnjak, E. Babić, I. Kušević, X. L. Wnag, S. Soltanian, S. X. Dou, *Solid State Commun.* **2007**, *143*, 412.

[10] E. W. Collings, M. D. Sumption, M. Bhatia, M. A Susner, S. D. Bohnenstiehl, *Supercond. Sci. Technol.* **2008**, *21*, 103001(14pp) and ref. therein.

[11] S. X. Dou, O. Shcherbakova, W. K. Yeoh, J. H. Kim, S. Soltanian, X. L. Wang, C. Senatore, R. Flukiger, M. Dhalle, O. Husnjak, E. Babic, *Phys. Rev. Lett.* **2007**, *98*, 097002.

[12] J. H. Kim Y.-U. Heo, A. Matsumoto, H. Kumakura, M. Rindfleisch, M. Tomsic, S. X. Dou, *Supercond. Sci. Technol*. **2010**, *21*, 075014.

[13] V.V. Moshchalkov, J. Fritzsche, *Nanostructured Superconductors*, Singapore: World Scientific, **2011**, chapter 1.

[14] I. Lončarek, A. M. Tonejc, Ž. Skoko, N. Novosel, M. Mustapić, K. Zadro, *Croat. Chem. Acta* **2013**, *86*, 297.

[15] N. Novosel, S. Galić, D. Pajić, Ž. Skoko, I. Lončarek, M. Mustapić, K. Zadro, E. Babić, *Supercond. Sci. Technol.* **2013**, *26*, 065004-1-065004-9.

[16] N. Novosel, S. Galić, D. Pajić, Ž. Skoko, I. Lončarek, M. Mustapić, K. Zadro, E. Babić, *Supercond. Sci. Technol*. **2012**, *25*, 095018.

[17] N. Novosel, S. Galić, D. Pajić, Ž. Skoko, I. Lončarek, M. Mustapić, K. Zadro, E. Babić, *Supercond. Sci. Technol.* **2013**, *26*, 105024.

[18] E. Babić, N. Novosel, D. Pajić, S. Galić, K. Zadro, Đ. Drobac, *J. Magn. Magn. Mater.* **2016**, *400*, 88.

[19] Y. Sun, D. Yu, Z. Liu, T. Wang, J. He, J. Xiang, D. Zheng, Y. Tian, *Supercond. Sci. Technol.* **2007**, *20*, 261.

[20] M. Mustapić, J. Horvat, M. S. Hossain, Ž. Skoko, S. X. Dou, *Supercond. Sci. Techol.* **2013**, *26*, 2013 075013.

[21] M. Mustapić, J. Horvat, M. S. Hossain, Ž. Skoko, D. R. G. Mitchell, S. X. Dou, *Acta Mater.* **2014**, *70*, 298.

[22] M. Mustapić, J. Horvat, Ž. Skoko, M. S. A. Hossain, S. X. Dou, *Acta Mater.* **2014**, *80*, 457.

[23] S. X. Dou, S. Soltanian, Y. Zhao, E. Getin, Z. Chen, J. Horvat, *Supercond. Sci. Technol.* **2005**, *18*, 710.

[24] T. Kuroda, T. Nakane, H. Uematsu, K. Kumakura, *Supercond. Sci. Technol.* **2006**¸*19*, 1152.

[25] T. Kuroda, T. Nakane, H. Kumakura, *Physica C* **2009**, *49*, 9.

[26] Ž. Skoko , J. Popović, K. Dekanić, V. Kolbas, S. Popović, *J. Appl. Cryst* **2012**, *46*, 594.

[27] Q. Zhao, Y. Liu, Q. Shi, Z. Ma, Z. Gao, *J. All. Comp.* **2009**, *470*, 443.

[28] S. Panday, B. S. S. Daniel, P. Jeevanandam, *J. Magn. Magn. Mater*. **2011**, *323*, 2271 and references therein.

[29] Y. C. Liu, Q. T. Shi, N. Zhao, Z. Q. Ma, *J. Mater. Sci.: Mater. Electron* **2007**, *18*, 855.

DOI: 10.5562/cca2985

Croat. Chem. Acta **2017**, *90*(*1*), 37–51